Al Haj, Yazan; Soliman, Ahmed B.; Vapaavuori, Jaana; Elbahri, Mady

Carbon Aerogels Derived from Anion-Modified Nanocellulose for Adaptive Supercapacitor Performance

Published in:
Advanced Functional Materials

DOI:
10.1002/adfm.202313117

Published: 10/07/2024

Document Version
Publisher's PDF, also known as Version of record

ADVANCED FUNCTIONAL MATERIALS
www.afm-journal.de

Carbon Aerogels Derived from Anion-Modified Nanocellulose for Adaptive Supercapacitor Performance

Yazan Al Haj, Ahmed B. Soliman, Jaana Vapaavuori, and Mady Elbahri**

In the pursuit of developing advanced carbon aerogel (CA) supercapacitors, a rational design approach is introduced that utilizes often overlooked conjugated anions to modulate the properties of CAs. Ionic cross-linking of cellulose nanocrystal (CNC) aerogels ensures the preservation of structural integrity even after carbonization. Interestingly, anion selection not only influences the cross-linking and carbonization processes but also significantly modulates the electrochemical performance of the resulting CAs. This is found to be vital in optimizing the overall supercapacitor performance. Electro-assisted (EA) wetting of the electrodes procures an adaptive and progressive performance enhancement, heralding the advent of sustainable supercapacitors crafted from earth-abundant materials.

1. Introduction

The increasing global concern regarding the environmental crisis has accelerated the quest for renewable and sustainable energy storage solutions. As researchers seek efficient, high-capacity, and environmentally friendly materials, nanocellulose aerogels have emerged as a highly promising candidate.[1] Derived from cellulose, the most abundant biopolymer on Earth, nanocellulose aerogels possess exceptional properties and exhibit huge potential for various applications.[2,3] When transformed into carbon, they offer exceptional porosity, conductive frameworks, and controlled surface charges.[4,5] These characteristics have opened new avenues in the field of energy storage, particularly in the context of electrochemical double layer capacitors (EDLCs), making them an ideal candidate for next-generation supercapacitors.[6–8]

Nanocellulose, in general, is abundant in hydroxyl groups (—OH), which facilitates easy functionalization and allows for the tailoring of its microstructure through chemical and/or physical cross-linking.[9,10] This process yields hydrogel/aerogel composites with unique electrochemical characteristics.[11] Previous research has primarily focused on controlling the cross-linking of nanocellulose using various metal cations.[9,12–16] However, the impact of the counter anions in the hydrogel has been largely overlooked, and the inherent chemical nature of the aerogels made by using the same cross-linking cation but different anions remains underexplored. This aspect is crucial, as it can significantly influence the electrochemical properties of the aerogel and, consequently, the overall performance of the supercapacitor.

In this study, we aim to assess the critical role of residual anions on the electrochemical performance of carbon aerogels (CAs), fabricated via cation-induced cross-linking of cellulose nanocrystals (CNCs). This involves a meticulous control of pore size distribution and electrochemical responses, highlighting the direct correlation between the microstructure of carbon-based electrodes in EDLC and the physicochemical characteristics of ionic species within the selected electrolytes. Furthermore, we address the challenge of compromised electrochemical storage performance due to poor wettability in carbon-based supercapacitor electrodes.[17,18] To overcome this, we introduce the concept of electro-assisted (EA) wetting, an innovative approach that effectively tackles the super-hydrophobic nature of nanocellulose-based CAs. This strategy not only enhances electrode wettability for efficient electrolyte infiltration but also ensures optimal charge storage, thereby unlocking the full potential of these materials for high-performance, sustainable supercapacitor applications.

2. Results and Discussion

2.1. Physiochemical Characterizations of the Aerogels

2.1.1. Synthesis of Carbon Aerogels

The schematic representation of the main synthesis process for cross-linked carbon aerogels (CA-Ca) is shown in **Figure 1**. First,

Y. Al Haj, J. Vapaavuori
Department of Chemistry and Materials Science
School of Chemical Engineering
Aalto University
Kemistintie1, Espoo 02150, Finland
E-mail: jaana.vapaavuori@aalto.fi
A. B. Soliman, M. Elbahri
Nanochemistry and Nanoengineering, Department of Chemistry and Materials Science
School of Chemical Engineering
Aalto University
Kemistintie1, Espoo 02150, Finland
E-mail: mady.elbahri@aalto.fi

The ORCID identification number(s) for the author(s) of this article can be found under https://doi.org/10.1002/adfm.202313117

DOI: 10.1002/adfm.202313117

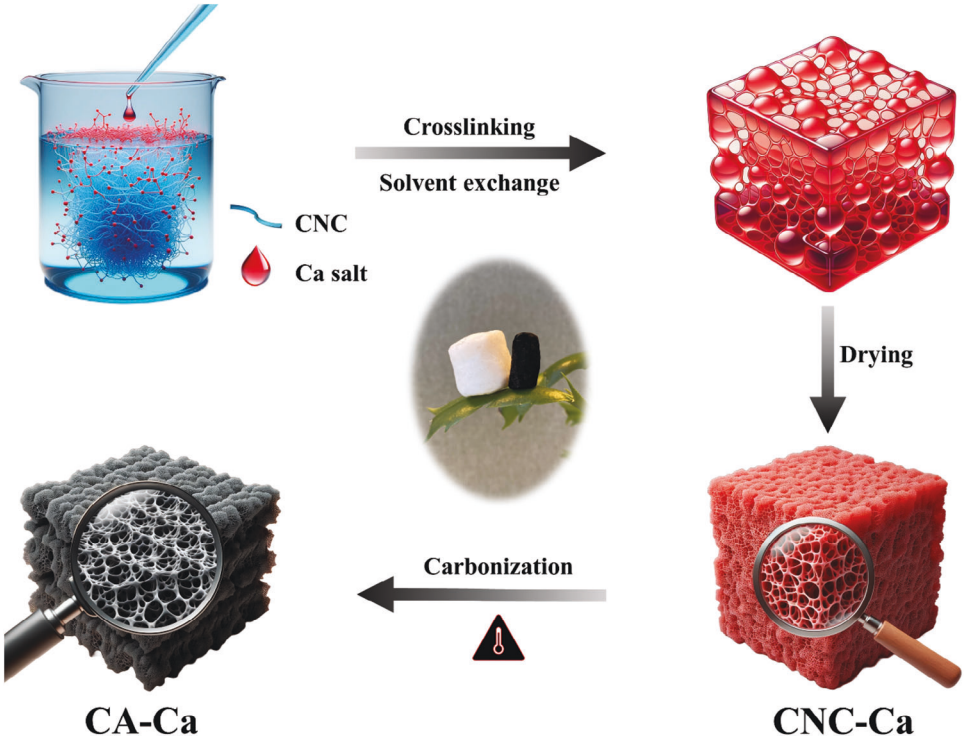

Figure 1. Schematic illustration of the synthesis of CA-Ca.

the CNCs suspension was sonicated in order to ensure good dispersibility before the addition of calcium salts (calcium acetate, calcium chloride, and calcium nitrate) to induce physical cross-linking. After complete cross-linking, solvent exchange took place, followed by supercritical drying and carbonization at 800 °C to obtain CA-Ace, CA-Chl, and CA-Nit, respectively. These will be used as electrode materials for supercapacitor applications.

2.1.2. Anionic Modulation of Physicochemical Properties of Carbon Aerogels

In order to elucidate the role of counter anions in modulating the properties of cation-cross-linked nanocellulose aerogels, a selection of anions with nearly similar ionic and hydration shells (Table S2, Supporting Information), but distinct hydration energies, was selected. This hydration energy serves as an indirect measure of the effective residual charge/ionic radii. Such control of the effective positive charges on the cation could thereby influence the strength of electrostatically driven cross-linking of the negatively charged colloidal CNC. The hydration energy trend observed was in the order of $Cl^- < CH_3COO^- < NO_3^-$.[20,21] As a result, the strength of Ca-induced cross-linking is expected to be inversely proportional to this order. Therefore, aerogels cross-linked with $Ca(NO_3)_2$ are hypothesized to exhibit a tighter pore system and greater overall surface area compared to those cross-linked with $Ca(OAc)_2$ and $CaCl_2$.

Indeed, the measured zeta potentials of CNC dispersions in the presence of the given anions were found to match the above-mentioned hypothesis. The pristine CNC (pCNC) was found to exhibit the highest zeta potential magnitude (−43.59 mV) indicating excellent resistance to aggregation and high colloidal stability. The addition of calcium salts as cross-linking agent into the pCNC suspensions resulted in a significant decrease in the magnitude of the zeta potential. The greatest reduction in the zeta potential was observed with $Ca(NO_3)_2$ where the CNC-Nit exhibited the lowest zeta potential value (−7.66 mV) compared to CNC-Ace (−8.74 mV) and CNC-Chl (−11.93 mV), suggesting weak repulsion forces between neighboring CNCs and a greater tendency to be cross-linked (**Figure** 2a). This tendency may lead to the formation of aerogels with smaller pores and higher surface area.[22]

Prior to the carbonization process, the specific surface area (SSA) values of the supercritically-dried samples were determined using the Brunauer-Emmet-Teller (BET) model. The results, including CNC-Nit, CNC-Ace, and CNC-Chl, are illustrated in Figure 2a and Figure S1 (Supporting Information). These values demonstrated a trend consistent with zeta potential findings. Furthermore, the resultant SSA/pore size distribution (PSD) illustrated in Figure 2b and Figure S2 (Supporting Information) of CAs after the carbonization process was found to follow the same trend. The SSA of CA-Ace, CA-Chl, CA-Nit, and CC-pCNC are 572, 518, 648, and 156 $m^2\ g^{-1}$, respectively (Figure 2b). All of the as-synthesized CAs exhibit a type-II-like isotherm with an H3-type hysteresis loop, indicating the presence of a mesoporous structure (according to IUPAC classification).[23] Additionally, the (PSD) analysis, as depicted in Figure S2 a,b (Supporting Information), indicates that among the dominant pore widths, CA-Nit exhibited the smallest value of 3.05 nm, while its counterparts peaked at 3.22, 3.31, and 81.3 nm, respectively. Furthermore, CA-Nit had the largest cumulative volume of pores at ≈0.60 $cm^3\ g^{-1}$,

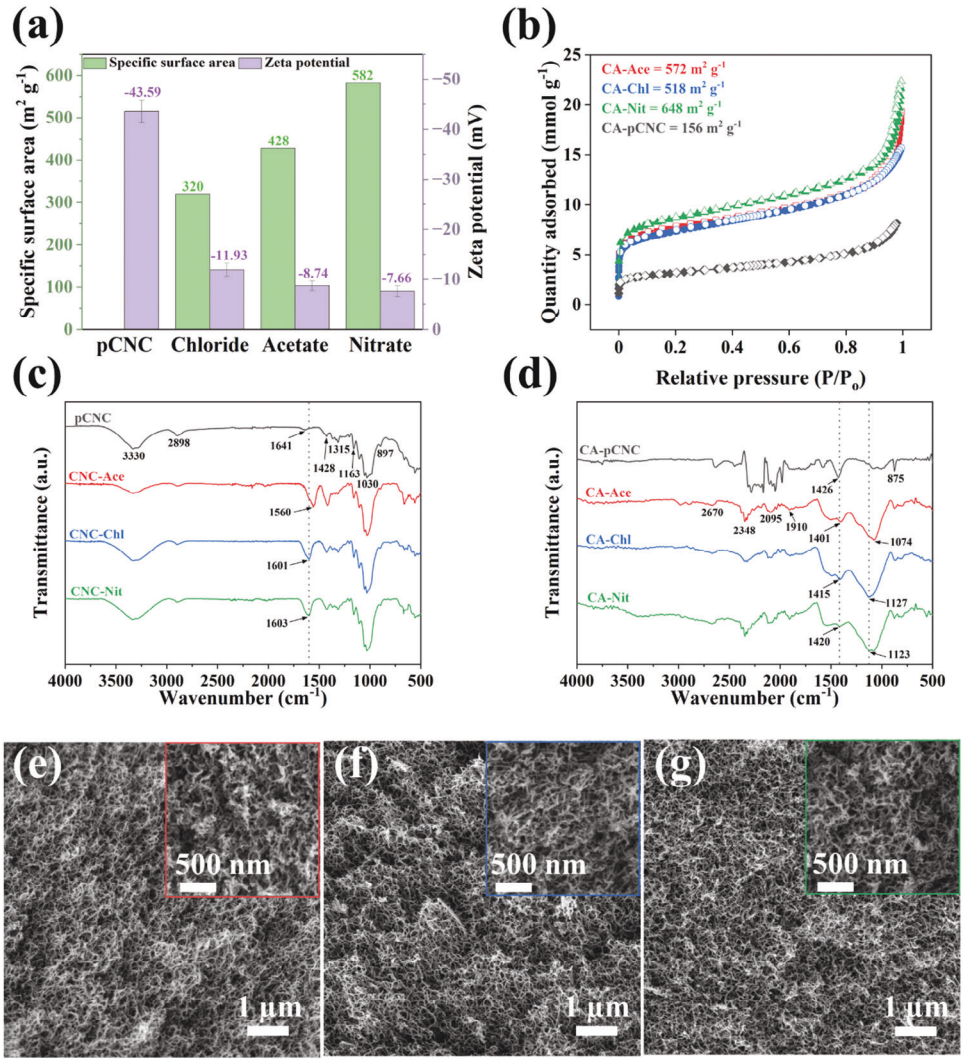

Figure 2. a) Specific surface area versus zeta potential for acetate, chloride, nitrate, and pCNC. b) N_2 sorption isotherm for CA samples, including CA-pCNC. FT-IR spectra c) before and after d) carbonization, respectively, and SEM images of e) CA-Ace, f) CA-Chl, and g) CA-Nit.

compared to CA-Ace (0.51 $cm^3\ g^{-1}$), CA-Chl (0.48 $cm^3\ g^{-1}$), and CC-pCNC (0.045 $cm^3\ g^{-1}$).

In order to trace changes in the surface functionalities of CNC during the cross-linking and carbonization processes, Fourier transform infra-red (FTIR) spectra were collected at various stages. Upon cross-linking, all samples preserved characteristic peaks associated with pCNC at 897, 1030, 1163, 1315 cm^{-1}, assigned to the stretching and anomeric vibration of glycosidic linkage, C—O, pyranose ring, C—O—C, C—O—H, respectively.[24] Upon addition of the metal salt, the only notable change observed was a shift in the asymmetric stretching vibrations of CNC carboxylate groups at 1641 cm^{-1} to lower wave numbers, accompanied by band broadening, indicating successful metal-induced cross-linking.[25] The carbonization involves multi-step dehydration and partial aromatization, leading to graphite-like structures. This is further confirmed by the elimination of free carboxylate and hydroxyl groups, as indicated by the diminishing of their characteristic bands at 1641 and 3330 cm^{-1} recorded for pristine CNC. Additionally, there was an intensification in the aromatic character and etheric linkages (doublet peak at 875 cm^{-1}) and a broadening of the 1074–1123 cm^{-1} band.[26]

The morphology of carbonized aerogels CA-Ace, CA-Chl, and CA-Nit was analyzed using scanning electron microscopy (SEM), as presented in Figure 2e–g. All images reveal a 3D porous network characterized by a nanoscale pore structure. Despite the variety of anions, no significant differences in nanostructure were observed, as indicated by the relatively similar pore size distributions across these samples. The uniformity is further confirmed by high-magnification insets in Figure 2e–g, showing no discernible individual calcium salt particles within the porous network. SEM imaging in Figure S3 (Supporting Information) demonstrates the structural integrity of CNC-Ca aerogels prior to carbonization, highlighting the effectiveness of cross-linking in maintaining the aerogel framework.

This preservation of structure contrasts with the control sample pCNC, and its carbonized form, CA-pCNC, as shown in Figure S4 (Supporting Information). The latter sample exhibits a significant structural degradation, highlighting the impact of

the carbonization process. The pCNC sample, initially displaying a 3D porous network, showed a collapsed structure after carbonization (in CA-pCNC). This structural deformation underscores the crucial role of cross-linking in preserving the aerogel structure under thermal stress. Such findings emphasize the necessity of cross-linking for maintaining structural integrity during high-temperature processing and its significant impact on the material's final properties. In contrast, SEM images of the CC-Nit (Figure S5, Supporting Information) show a collapsed structure with visible particles, indicative of the freeze-drying process, which tends to concentrate solutes and crystallize salt particles due to its unique physical drying mechanism, further illustrating the importance of preparation methods on aerogel integrity.[27] Density measurements corroborate these structural observations, with CA-Ca maintaining a significantly lower density (0.053 ± 0.0016 g cm^{-3}) compared to freeze-dried cryogels (0.212 ± 0.0037 g cm^{-3}).

The detailed elemental composition and oxidation states of all CA were further examined by XPS. The XPS spectra survey of all composites (Figure S6, Supporting Information) depicts the characteristic peaks of Ca, C, and O elements. The high-resolution Ca 2p spectrum (Figure S7a–d, Supporting Information) can be deconvoluted into two species at 347.8 ± 0.3 and 351.3 ± 0.3 eV, ascribed to Ca $2p_{3/2}$ and $2p_{1/2}$, respectively which can be attributed to Ca(II) in either $CaCO_3$ or $CaSO_4$ forms.[28] As indicated in Figure S8a–d (Supporting Information), the carbon spectra (C 1s) for all the samples show C═C, C─O, and O═C═O bonds with centralized binding energy at ≈284.5, 285.4, and 289.0 eV, respectively.[29] In addition, the O1s peaks for all CA were fitted to three peaks at ≈531.8 eV ascribed for C═O, at ≈532.7 eV deconvoluted for C─O, and a third peak at ≈535.3 eV assigned to oxygen and/or water adsorption on the sample surface, as shown in Figure S9a–d (Supporting Information).[30] It is worth mentioning that the observed shifts in the Ca/O binding energies can be attributed to the various polymorphs having different electronic configurations, as previously noted in the literature.[31]

When considered together, these findings highlight, first, the contribution of cation cross-linking for preserving the structural integrity of the aerogel in the carbonization process and, second, the significance of anions to fine-tuning the porosity of the aerogels. The hierarchical mesoporous structure, with a large SSA, small average pore size, and considerable cumulative volume of pores, provides abundant ion adsorption sites and shortens the ion transmission pathway within the CA network.[32,33] This highly porous nanostructure optimizes ion/electron transport pathways, enhancing the electrochemical performance when used as electrodes for supercapacitors, a feature that will be elucidated further in this study.

2.2. Electrochemical Evaluation

2.2.1. Electrochemical Performance and Charge Electrolyte Interaction

To investigate the potential of CNC-derived carbon aerogels as an active material for EDLC, the electrochemical performance of CA-Ca was evaluated by cyclic voltammetry (CV) and galvanic charge/discharge (GCD) techniques. For these experiments, CA-Ca was drop-cast on a graphite rod as the working electrode, aqueous 0.5 M H_2SO_4 was used as the electrolyte, Pt coil as the counter electrode, and Ag/AgCl as the reference electrode. **Figure 3**a displays the CV curves of CA-Ace, CA-Chl, CA-Nit, and bare graphite electrode at a constant scan rate of 100 mV s^{-1} with an operating potential of 0–0.8 V (vs Ag/AgCl). The CV curve for bare graphite exhibits an exceptionally low current density in comparison to those of the CA-Ca electrodes, indicating that the capacitive performance of the active material remains largely unaffected under identical electrochemical measurements. All the CV curves exhibit a nearly rectangular shape, indicating ideal EDLC behavior. Generally, the specific capacitance of the electrode material can be estimated by the area of the CV curves. Impressively, the CA-Nit electrode displays a larger voltammogram area compared to those of CA-Ace and CA-Chl, suggesting the enhancement in the electrochemical performance. This enhanced performance is likely due to a higher electrochemically active surface area for ion adsorption and an excellent porous structure, which is consistent with BET and PSD analysis.[34,35] Figure S10a–c (Supporting Information) depicts the CV curves of the obtained materials at scan rates from 5 to 400 mV s^{-1}, showing a significant increase in current density at higher rates and a consistent CV shape, which suggests stable capacitive behavior of CA-Ca electrodes.

Figure 3b displays the GCD curves for the evaluated CA-Ca at 1 A g^{-1} within the potential window of 0.1–0.8 V versus Ag/AgCl. Even at higher current densities (from 1 to 20 A g^{-1}), all the GCD curves clearly exhibit linear and symmetrical behavior, characteristics of EDLC, which is in good agreement with CV analysis (Figure S11a–c, Supporting Information). At a current density of 1 A g^{-1}, the CA-Nit had the longest discharge time (289 s) in comparison to CA-Ace (230 s) and CA-Chl (209 s), implying higher specific capacitance (**Table 1**). The specific capacitance of the CA-Nit electrode was determined by analyzing the GCD curves using Equation 2. At a current density of 1 A g^{-1}, CA-Nit demonstrated a significantly higher specific capacitance (413.3 F g^{-1}) than both CA-Ace (328.1 F g^{-1}) and CA-Chl (298.2 F g^{-1}), as depicted in Figure 3c. Remarkably, as shown by Table S1 (Supporting Information), this synthesis method outperforms other cellulose-derived carbon aerogel electrodes, yielding supercapacitors with excellent performance.

The energy density and power density of the characterized CA-Ca were calculated using Equations 3 and 4, respectively, and presented in Table 1. All obtained samples exhibit a high power density ≈350 W kg^{-1}, while CA-Nit possesses a superior energy density of ≈28.1 Wh kg^{-1} compared to its counterparts. The results indicate that a highly effective and simple method has been developed to fine-tune the porosity and pore sizes, thereby tailoring the performance of supercapacitors.

The electrochemical performance of supercapacitors is known to be significantly influenced by several factors. First, the pore size distribution of the electrode material plays a critical role in determining the specific surface area, accessibility of electrolyte ions to the surface, and charge storage capacity.[36] Second, the surface functional groups of carbon materials provide specific surface chemistry, facilitating the adsorption and desorption of electrolyte ions.[37] Last, the size of electrolyte ions affects the diffusion rate of ions into the electrode material, thereby

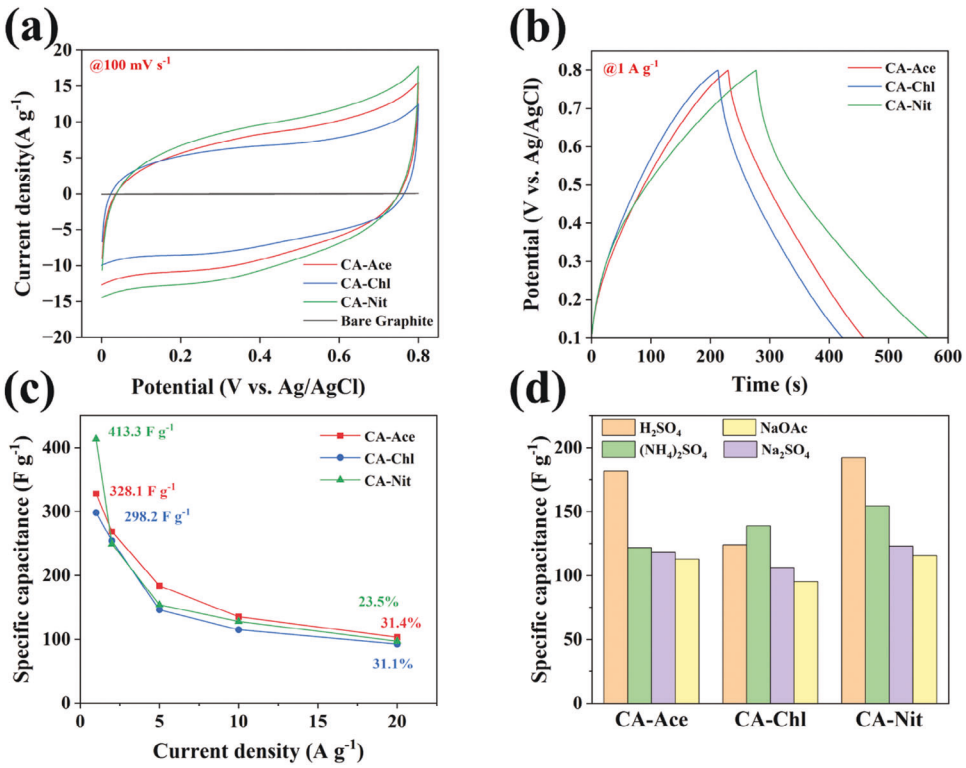

Figure 3. Electrochemical performance of CA-Ace, CA-Chl, and CA-Nit: a) CV curves at 100 mV s^{-1}, b) GCD curves at 1 A g^{-1}, c) The corresponding specific capacitance at different current densities (1–20 A g^{-1}), and d) Specific capacitance at 5 mV s^{-1} using different electrolytes within the potential window of 0–0.8 V.

impacting the charge/discharge rate and overall performance of supercapacitors.[38]

In this context, a set of pre-selected electrolytes with different ionic radii/charges including $(NH_4)_2SO_4$, Na_2SO_4, and NaOAc were utilized to probe the electrochemical accessiblemicrostructure(s) of the prepared aerogels emphasizing their electrochemical double layer structures and residual surface charges. The cyclic voltammograms in Figures S12–S15 (Supporting Information) validate that the capacitive nature of the EDLC-based capacitor varies significantly with different electrolytes, even when using the same active material. This variation is due to several factors, including the ionic radius, size of hydrated ions, ionic conductivity, and ion mobility in the solution (Table S2, Supporting Information). For example, hydrated ion radius follows the order: H^+ < NH_4^+ < Na^+, although the radii typically range between 2.8 and 3.8 Å, other factors might influence electrochemical performance more significantly. Ionic conductivity and mobility also define the behavior of different electrolytes, with H^+ ions exhibiting the highest conductivity among cations at 349.8 S cm^2 mol^{-1}, and SO_4^{2-} ions leading among anions at ≈160.0 S cm^2 mol^{-1}. Consequently, the descending order of conductivity for the evaluated electrolytes is: H_2SO_4 > $(NH_4)_2SO_4$ > Na_2SO_4 > NaOAc.

The CV potential window was set between 0 and 0.8 V. Using a positive bias to charge/discharge the electrode material facilitated the investigation of the diffusion impact of anionic charge carriers within the electrode pore(s). Figure 3d shows that in the case of the CA-Ace, the electrode was nearly insensitive to the different electrolyte options except for H_2SO_4, indicating the hidden role of the H^+ to trigger the full charging capacity of the material through altering its double layer structure. Furthermore, it confirms the mesoporous structure of the CA-Ace is the main reason beyond its suboptimal performance. In contrast, both CA-Chl and CA-Nit electrodes exhibit high sensitivity to the ionic radii and charge of the overall ionic species in the electrolyte solution. They both show the same capacitance trend: NaOAc < Na_2SO_4 < $(NH_4)_2SO_4$, which is consistent with the consideration of both anion and cation sizes. Surprisingly, the capacitance trends for CA-Chl and CA-Nit are completely opposite when using H_2SO_4 as the electrolyte. This divergence suggests that the charge storage mechanism is influenced by multiple factors. It is controlled not only by the double-layer structure, but also by the size of the hydrated cations, as evidenced in Tables S2,S3 (Supporting Information). Accordingly, the overall performance of the cellulose-derived CA is not only governed by the ultimate surface area/PSD but also via careful selection of the associated

Table 1. Electrochemical performance of CA-Ca obtained from GCD at 1 A g^{-1}.

Sample	Δt [s]	ΔV [V]	C_S [F g^{-1}]	E [Wh kg^{-1}]
CA-Ace	230	0.7	328.1	22.4
CA-Chl	209	0.7	298.2	20.3
CA-Nit	289	0.7	413.3	28.1

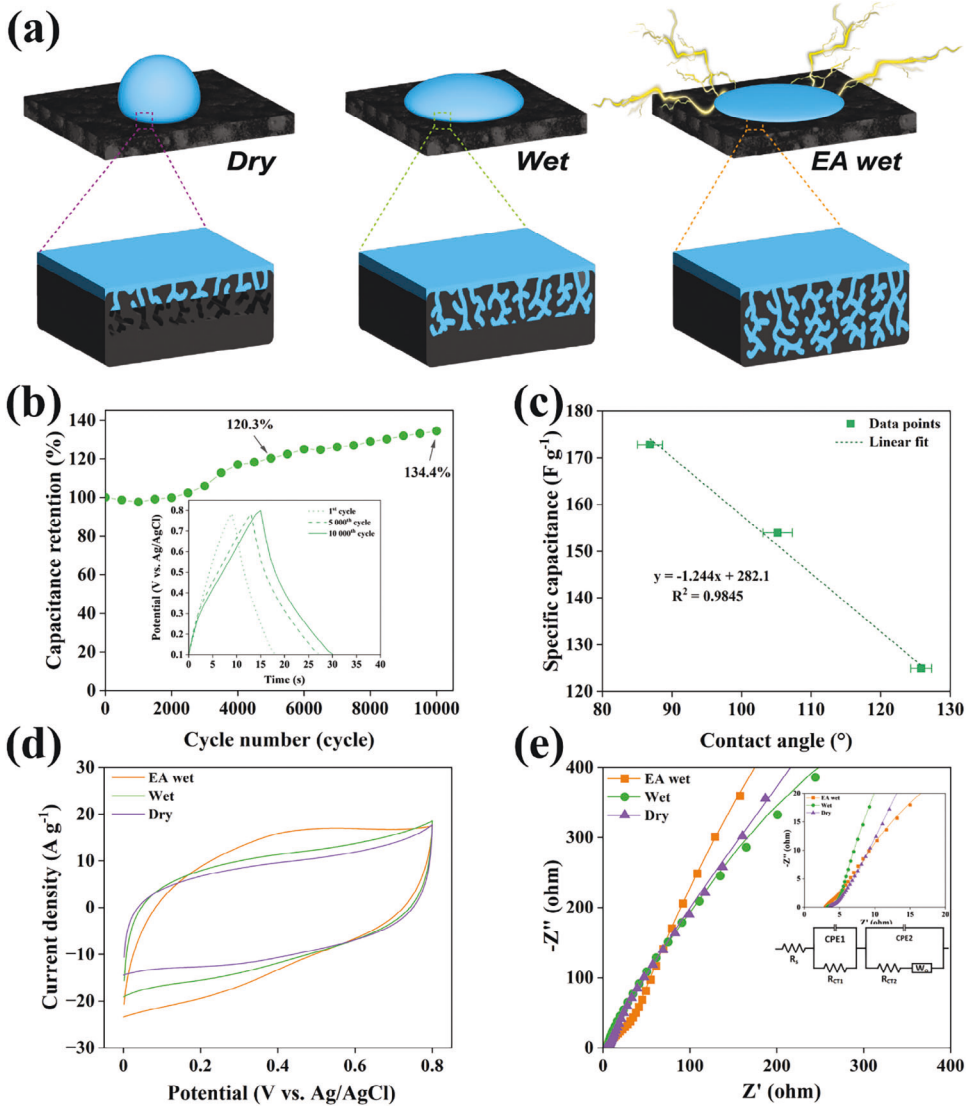

Figure 4. a) Schematic illustration of the electrodes under dry, wet, and EA wet conditions, b) Cyclic performance after 10 000 consecutive charge-discharge cycles at 10 A g^{-1} (inset shows the corresponding GCD curves of 1st, 5000th, and 10 000th cycle), c) linear fitting of the specific capacitance as a function of contact angle, d) CV curves of CA-Nit under EA wet, wet, and dry conditions at 100 mV s^{-1}, and e) Nyquist impedance plots (inset: magnified view of the high-frequency region and equivalent circuit model).

electrolyte that matches such EDLC capacitive charge storage systems.[39]

2.2.2. Unleashing the Potential: Progressive Supercapacitor Performance and Stability

Performance consistency and stability are essential for supercapacitor reliability and longevity. Historically, the search for high-performing materials for EDLC supercapacitors has predominantly emphasized materials with extensive surface areas, neglecting other influential factors. In this study, we explore the role of surface wettability, introducing the concept of electro-assisted adaptive wettability and its significant impact on the electrolyte accessible surface area portion. Electro-assisted (EA) electrode wetting is a process in which the electrode undergoes multiple cyclic treatments or conditionings to achieve permanent and adaptive wettability without continuous applied potential. The aim of these treatments is to modify the surface properties of the electrode material, ensuring consistent optimal wetting behavior even in the absence of an external electric field (**Figure** 4a). This approach significantly improves the performance and reliability of supercapacitors and associated electrochemical devices. The enhanced material capacitance associated with electro-assisted wetting can be attributed to the forced, electro-driven diffusion of electrolyte ionic species within the narrow pore system, effectively overcoming diffusion barriers. These barriers are analogous to a series of resistors. When an electric field is applied, ions are enabled to penetrate even the

narrower pores, facilitated by forced diffusion and electrosorption mechanisms.[40]

The cycling stability of CA-Nit was evaluated over 10 000 charge-discharge cycles at 10 A g^{-1}. As depicted in Figure 4b, capacitance retention reached 120.29% and 134.42% after 5000 and 10 000 cycles, respectively. These findings emphasize the superior cycling stability and consistent performance enhancement of CA-Nit, outperforming other cellulose-based carbon aerogels (Table S1, Supporting Information). The SEM images (Figure S16, Supporting Information) confirm that the morphological structure of CA-Nit remained stable and intact even after extensive cycling tests, demonstrating its robust structural integrity under strenuous working conditions. Wettability assessments at various cycles (Figure S17, Supporting Information) revealed a reduction in contact angle from ≈130.83° to 85.37° after 10 000 cycles, aligning with increases in specific capacitance to ≈124.9, 154, and 172.8 F g^{-1} at 1000, 5000, and 10 000 cycles, respectively. A distinct linear relationship between contact angle and specific capacitance is evident, hinting at the possibility of achieving peak capacitance with complete super-hydrophilic wetting (Figure 4c).

To validate the hypothesis, further investigations were undertaken to assess the influence of the wetting stage on the electrochemical performance of CA-Nit. The material was applied to three distinct graphite rods and subsequently evaluated using CV, GCD, and EIS techniques. The "dry" electrode was left as cast, the "wet" electrode was immersed in 0.5 M H_2SO_4 for 24 h, and the "EA wet" electrode underwent 10 000 cycles (≈67 h). Figure 4d and S18 (Supporting Information) depict the CV and GCD curves for each electrode. A clear correlation emerged, indicating that enhanced wettability leads to improved electrochemical performance. Specific capacitance values, derived from the CV and GCD data, were 94.4 and 128 F g^{-1} for the dry condition, 109.4 and 149.8 F g^{-1} for the wet condition, and 130.7 and 172.8 F g^{-1} for the EA wet condition, at scan rates of 100 mV s^{-1} and current densities of 10 A g^{-1}, respectively (Figure S19, Supporting Information).

To better understand the mechanisms behind the improved specific capacitance in wetted samples, electrochemical impedance spectroscopy (EIS) was utilized. Figure 4e, depicts the Nyquist plots of EA wet, wet, and dry electrodes. The EIS results for all three electrodes were fitted using the same equivalent circuit, which is displayed as an inset in Figure 4e, and the corresponding data are provided in Table S4.(Supporting Information)

In the high-frequency region, the system impedance was primarily influenced by the internal and interfacial resistances of the electrodes, as well as the ohmic resistance of the electrolyte, denoted by the resistor component (R_s). This region also exhibits a semicircle impedance pattern, representing interface resistance (R_{CT-1}) and constant phase element (CPE) indicative of the double layer capacitance. Most importantly, both R_s and R_{CT-1} exhibit a decrease as electrode wettability increases, with the EA wet electrode achieving the lowest values at 3.002 and 0.332 Ω, respectively, compared to its counterparts (Table S4, Supporting Information). These results align well with the contact angle measurements and electrochemical CV and GCD findings.

In the low-frequency region, the straight line represents ion diffusion process within the porous aerogel network. This is attributed to the Warburg element (W_o) along with a second time constant (CPE2).[41] However, the primary focus is on the B parameter, which represents the diffusion time within the porous network. These values indicate that the diffusion process is fastest for the EA wet electrode, with a diffusion time constant of only 0.622 $sec^{0.5}$. In contrast, the wet and dry electrodes exhibit considerably lengthier diffusion times, measuring at 7.277 and 9.776 $sec^{0.5}$, respectively. These varying values underscore the significant influence of electro-assisted wetting on diffusion rates, ultimately contributing to the attainment of optimal electrochemical performance.

Our findings emphasize the significant and often overlooked influence of wettability, especially electro-assisted wettability, on the electrochemical performance of materials. This exploration suggests that we might currently be harnessing only ≈40% of a material's ultimate performance due to suboptimal wettability, urging a re-assessment of EDLC supercapacitor material strategies. The application of this study is currently limited to the EDLC carbon-based electrodes, where the device performance is influenced by the complex nature of ion diffusion and electrosorption phenomena and their role in the double layer structure of porous electrodes. However, further research is needed to extend these concepts to redox-mediated pseudo/hybrid capacitor electrodes, where the chemical involvement of ionic species becomes more dominant. Additionally, more studies addressing the challenges related to scalability, mass production, and processing times are essential for practical industrial-scale applications.

To further examine the practical energy storage applications of CA-Nit, a systematic electrochemical characterization was performed on a symmetric supercapacitor. This setup utilized graphite sheets as current collectors, a glass fiber separator, and a 0.5 M H_2SO_4 electrolyte. The characterization encompassed CV conducted across a range of scan rates from 25 to 400 mV s^{-1} and GCD at various current densities ranging from 0.1 to 5 A g^{-1}, all within a potential window of 0–1.0 V. The resulting CV and GCD curves are presented in Figure S20a,b (Supporting Information), respectively, revealing distinctive double-layer capacitor behavior. The supercapacitor achieved a specific capacitance of ≈139.9 F g^{-1} at 0.1 A g^{-1} (Figure S20c, Supporting Information) and maintained ≈39% of this value at a higher current density of 5 A g^{-1}. Furthermore, an assessment of long-term cyclic stability was conducted over 13 000 charge-discharge cycles at a scan rate of 200 mV s^{-1}, showcasing an impressive capacitance retention of ≈111.4% (Figure S20d, Supporting Information). This result highlights the exceptional cyclic stability of the device, which is in alignment with our presented findings from studies involving three-electrode systems and wettability tests.

The energy and power densities were evaluated and are represented in the Ragone plot (Figure S20e, Supporting Information). The supercapacitor exhibited exceptional performance, achieving an energy density of 19.4 Wh kg^{-1} at a power density of 109.3 W kg^{-1}, while maintaining a high energy density of 9.8 Wh kg^{-1} even at an elevated power density of 4371.6 W kg^{-1}. These results, particularly in terms of cyclic stability and energy/power densities, surpass the performance of numerous cellulose-derived carbon aerogels documented in the literature, as comprehensively detailed in Table S5 (Supporting Information).

3. Conclusion

In this study, we investigated the impact of various salt anions–including calcium chloride, calcium nitrate, and calcium acetate – on the structural and electrochemical properties of CA-Ca for supercapacitor applications. Our findings demonstrate that the type of salt used significantly affects the SSA and pore size distribution, which in turn influences the electrochemical performance of the supercapacitor. Specifically, calcium nitrate resulted in the highest SSA, smallest dominant pore size, and superior electrochemical performance across various electrolytes. We also examined the effect of wettability on electrochemical performance and found that greater EA wettability was associated with the improved overall performance of the supercapacitor. Overall, these results contribute to a better understanding of the factors that influence the performance of supercapacitors and can guide the development of improved energy storage devices.

4. Experimental Section

Materials and Chemicals: Spray-dried cellulose nanocrystals (CNCs) powder was provided by CelluForce Inc. (Montreal, Canada). Calcium acetate ($Ca(OAc)_2$), calcium chloride ($CaCl_2$), calcium nitrate ($Ca(NO_3)_2$), 2-Propanol, Nafion solution, Polytetrafluoroethylene (PTFE) dispersion (60 wt.%), sulfuric acid (H_2SO_4, 98.0%), ammonium sulfate ($(NH_4)_2SO_4$, ≥99.0%), sodium sulfate (Na_2SO_4, ≥99.0%), and sodium acetate (NaOAc, ≥99.0%) were purchased from Sigma–Aldrich (Germany). All chemicals were used without any further purification.

Preparation of Cross-Linked Carbon Aerogels (CA-Ca): An aqueous suspension of commercial CNCs was prepared by dispersing CNC powder in DI water (2 wt.%). After stirring overnight, the CNC suspension was first sonicated for 15 min and then poured into a custom-made cylinder-shaped Teflon mold (with a volume of 25 cm^3). Subsequently, calcium acetate, calcium chloride, and calcium nitrate (50 mM) were added dropwise separately to the previous suspension and kept overnight, to ensure complete cross-linking. The obtained hydrogels were designated as "CNC-Ace", "CNC-Chl", and "CNC-Nit", respectively. Prior to supercritical drying, the hydrogels were solvent-exchanged stepwise with ethanol. Afterward, the dried hydrogels (aerogels; CNC-Ca) were carbonized at 800 °C for 2 h (ramp rate of 5 °C min^{-1}) in a nitrogen atmosphere. The obtained CA were designated as "CA-Ace", "CA-Chl", and "CA-Nit", respectively. To investigate the effects of cross-linking and drying methods, two control samples were prepared. The first, CA-pCNC, was a pristine CNC aerogel prepared identically to the original samples but without the addition of any cross-linking agent. The second, CC-Nit, a CNC cryogel cross-linked with calcium nitrate, followed the same preparation steps as the original samples, with the exception that supercritical drying was replaced by freezing the sample at −150 °C and subsequent freeze-drying.

Attenuated Total Reflectance Fourier Transform Infrared (ATR-FTIR) Spectroscopy: The surface chemistry of CNC-Ca and CA-Ca was characterized at room temperature using Spectrum Two FT-IR spectrometer (PerkinElmer, USA), equipped with a diamond attenuated total reflectance (ATR). To avoid the effect of humidity, the samples underwent vacuum drying at 60 °C overnight prior to conducting the measurements. The spectra were measured between 4000 and 500 cm^{-1} at a resolution of 2 cm^{-1} and averaged on three scans.

Scanning Electron Microscopy (SEM): The morphology of the obtained CA-Ca was observed by SEM using TESCAN MIRA 3 (Brno, Czech Republic) at an accelerating voltage of 5.0 kV at room temperature. Prior to observation, a 5 nm thick gold-palladium (Au-Pd) coating was sputtered.

Zeta Potential: The zeta potential was measured using Zeta sizer Nano ZS 90 (Malvern Panalytical, UK) at 25 °C. In detail, the CNC suspension was diluted to 0.1 wt.% before adding 50 mM of calcium salt. For pCNC, no salt was added to CNCs suspension. Each sample was examined five times.

Nitrogen Sorption Isotherms: The specific surface area and pore size distribution of the obtained materials were measured at a temperature of 77 K using Micromeritics TriStar II (Georgia, US).for carbonized samples and a BELSORP-max II for control and non-carbonized samples. Prior to measurements, the samples were pre-treated using Micromeritics FlowPrep at 120 °C for 2 h under nitrogen flow, while non-carbonized samples were pre-treated at 80 C for 12 h under nitrogen flow.

X-Ray Photoelectron Spectroscopy (XPS): The surface chemical analysis of the CA-Ca was examined using Kratos AXIS Ultra XPS (Manchester, UK) with an Al Kα X-ray source (1486.6 eV). The survey spectra were recorded at a pass energy of 20 eV.

Bulk Density: The bulk densities (ρ_b) of carbonized aerogels and cryogels were calculated using Equation 1:

$$\rho_b = \frac{m}{V} \tag{1}$$

where m and V are the weight and volume of the sample, respectively.

Contact Angle Measurements: The wettability of the CA-Ca samples was measured using Theta Flex Biolin Scientific (Stockholm, Sweden) by static contact angle mode. A 5 µL droplet of DI water was deposited on the surface at room temperature, and images were taken after 10 s of stabilization. The measurements were repeated three times for each sample.

Electrochemical measurements: The electrochemical performance of the obtained CA was examined in a three-electrode setup using Pt coil as counter electrode, Ag/AgCl as reference electrode, and graphite rod as working electrode. A slurry of active material was prepared by adding 10 mg of obtained CA to 1 mL of 2-propanol and 30 µL of Nafion solution. After sonication, 10 µL of the previous slurry was drop cast on a graphite rod and used as a working electrode. All three-electrode setup measurements were conducted in 0.5 M aqueous electrolytes, including H_2SO_4, $(NH_4)_2SO_4$, Na_2SO_4, and NaOAc. The cyclic voltammetry (CV), galvanostatic charge-discharge (GCD), and electrochemical impedance spectroscopy (EIS) were all conducted using a Gamry Potentiostat/Galvanostat/ZRA. The specific capacitance (C_S, F g^{-1}) of the active material was calculated from GCD curves using Equation 2[19]:

$$C_S = \frac{i\,(\Delta t)}{m\,(\Delta V)} \tag{2}$$

where i is the current while discharging process (A), Δt is the discharging time (s), m is the mass of electrode material loading (g), and ΔV is the potential window (V). The energy density (E, Wh kg^{-1}) and power density (W kg^{-1}) were calculated using the following equations:[19]

$$E = \frac{1}{2}\, C_S\, (\Delta V)^2 \tag{3}$$

$$P = \frac{E}{\Delta t} \tag{4}$$

Following the three-electrode analysis, a symmetric two-electrode system was evaluated. The electrodes were prepared by coating 1 × 1 cm^2 graphite sheets (each with 1 mg active material) with CA-Nit ink, which was formulated using a mixture of 75 wt.% active material, 10 wt.% carbon black, 15 wt.% PTFE dispersion, and ethanol as the solvent. Prior to the measurements, both electrodes and a glass fiber separator were immersed in 0.5 M H_2SO_4 electrolyte for 24 h. The final assembly was then securely wrapped in Teflon tape, effectively preventing any leakage or evaporation of the electrolyte.

Supporting Information

Supporting Information is available from the Wiley Online Library or from the author.

Acknowledgements

Y.A.H. and A.B.S. contributed equally to this work. Y.A.H. and J.V. acknowledge the generous funding from the Academy of Finland's Flagship Programme under Projects No. 318890 and 318891 (Competence Center for Materials Bioeconomy, FinnCERES).

Conflict of Interest

The authors declare no conflict of interest.

Data Availability Statement

The data that support the findings of this study are available from the corresponding author upon reasonable request.

Keywords

carbon aerogels, cellulose nanocrystals, electro-assisted wetting, physical cross-linking, supercapacitors

Received: October 23, 2023
Revised: January 23, 2024
Published online: March 11, 2024

[1] C. Chen, L. Hu, *Acc. Chem. Res.* **2018**, *51*, 3154.
[2] S. Zhao, W. J. Malfait, N. Guerrero-Alburquerque, M. M. Koebel, G. Nyström, *Angew. Chemie–Int. Ed.* **2018**, *57*, 7580.
[3] H. Liu, T. Xu, C. Cai, K. Liu, W. Liu, M. Zhang, H. Du, C. Si, K. Zhang, *Adv. Funct. Mater.* **2022**, *32*, 2113082.
[4] L. Chen, H. Yu, Z. Li, X. Chen, W. Zhou, *Nanoscale* **2021**, *13*, 17837.
[5] Z. Bi, Q. Kong, Y. Cao, G. Sun, F. Su, X. Wei, X. Li, A. Ahmad, L. Xie, C. M. Chen, *J. Mater. Chem. A* **2019**, *7*, 16028.
[6] W. Chen, H. Yu, S. Y. Lee, T. Wei, J. Li, Z. Fan, *Chem. Soc. Rev.* **2018**, *47*, 2837.
[7] A. V. Patil, S. A. Sawant, R. G. Sonkawade, R. S. Vhatkar, *J. Energy Storage* **2023**, *72*, 108533.
[8] C. Zhang, H. Wang, Y. Gao, C. Wan, *Mater. Des.* **2022**, *219*, 110778.
[9] K. J. De France, T. Hoare, E. D. Cranston, *Chem. Mater.* **2017**, *29*, 4609.
[10] L. Dai, Y. Wang, W. Li, W. Zhao, C. Duan, C. Xiong, Y. Ni, *J. Power Sources* **2021**, *493*, 229711.
[11] Y. Al Haj, S. Mousavihashemi, D. Robertson, M. Borghei, T. Pääkkönen, O. J. Rojas, E. Kontturi, T. Kallio, J. Vapaavuori, *Chem. Eng. J.* **2022**, *435*, 135058.
[12] F. Zou, T. Budtova, *Carbohydr. Polym.* **2021**, *266*, 118130.
[13] M. Chau, S. E. Sriskandha, D. Pichugin, H. Thérien-Aubin, D. Nykypanchuk, G. Chauve, M. Méthot, J. Bouchard, O. Gang, E. Kumacheva, *Biomacromolecules* **2015**, *16*, 2455.
[14] J. J. Kaschuk, Y. Al Haj, O. J. Rojas, K. Miettunen, T. Abitbol, J. Vapaavuori, *Adv. Mater.* **2021**, *34*, 2104473.
[15] F. Doustdar, A. Olad, M. Ghorbani, *Int. J. Biol. Macromol.* **2022**, *208*, 912.
[16] C. A. Maestri, P. Bettotti, M. Scarpa, *J. Mater. Chem. B* **2017**, *5*, 8096.
[17] A. Gopalakrishnan, S. Badhulika, *J. Power Sources* **2020**, *480*, 228830.
[18] C. Liu, X. Yan, F. Hu, G. Gao, G. Wu, X. Yang, *Adv. Mater.* **2018**, *30*, 1705713.
[19] L. Q. Mai, A. Minhas-Khan, X. Tian, K. M. Hercule, Y. L. Zhao, X. Lin, X. Xu, *Nat. Commun.* **2013**, *4*, 3923.
[20] R. Epsztein, E. Shaulsky, N. Dizge, D. M. Warsinger, M. Elimelech, *Environ. Sci. Technol.* **2018**, *52*, 4108.
[21] A. Ghorbani1, B. Bayati, T. Poerio, P. Argurio, T. Kikhavani, M. Namdari, L. M. Ferreira, *Molecules* **2020**, *25*, 4911.
[22] R. Prathapan, R. Thapa, G. Garnier, R. F. Tabor, *Colloids Surf. A Physicochem. Eng. Asp.* **2016**, *509*, 11.
[23] Y. Al Haj, J. Balamurugan, N. H. Kim, J. H. Lee, *J. Mater. Chem. A* **2019**, *7*, 3941.
[24] A. G. Dumanlı, A. H. Windle, *J. Mater. Sci.* **2012**, *47*, 4236.
[25] X. Liu, Y. Jiang, Y. Wei, X. Wei, *Mater. Des.* **2022**, *224*, 111431.
[26] V. Ţucureanu, A. Matei, A. M. Avram, *Crit. Rev. Anal. Chem.* **2016**, *46*, 502.
[27] G. Zu, J. Shen, L. Zou, F. Wang, X. Wang, Y. Zhang, X. Yao, *Carbon* **2016**, *99*, 203.
[28] B. Demri, D. Muster, *J. Mater. Process. Technol.* **1996**, *55*, 311.
[29] B. M. Lee, J. J. Eom, G. Y. Baek, S. K. Hong, J. P. Jeun, J. H. Choi, J. M. Yun, *Cellulose* **2019**, *26*, 4529.
[30] K. Ishimaru, T. Hata, P. Bronsveld, D. Meier, Y. Imamura, *J. Mater. Sci.* **2007**, *42*, 122.
[31] M. Ni, B. D. Ratner, *Surf. Interface Anal.* **2008**, *40*, 1356.
[32] N. Ramirez, D. Zámbó, F. Sardella, P. A. Kißling, A. Schlosser, R. T. Graf, D. Pluta, C. Deiana, N. C. Bigall, *Adv. Mater. Interfaces* **2021**, *8*, 2100310.
[33] H. Li, J. Li, A. Thomas, Y. Liao, *Adv. Funct. Mater.* **2019**, *29*, 1904785.
[34] Y. Gao, S. Zheng, H. Fu, J. Ma, X. Xu, L. Guan, H. Wu, Z. S. Wu, *Carbon* **2020**, *168*, 701.
[35] B. Thomas, G. George, A. Landström, I. Concina, S. Geng, A. Vomiero, M. Sain, K. Oksman, *ACS Appl. Electron. Mater.* **2021**, *3*, 4699.
[36] L. Zhang, X. S. Zhao, *Chem. Soc. Rev.* **2009**, *38*, 2520.
[37] E. Frackowiak, F. Béguin, *Carbon* **2001**, *39*, 937.
[38] C. Zhong, Y. Deng, W. Hu, J. Qiao, L. Zhang, J. Zhang, *Chem. Soc. Rev.* **2015**, *44*, 7484.
[39] B. Pal, S. Yang, S. Ramesh, V. Thangadurai, R. Jose, *Nanoscale Adv* **2019**, *1*, 3807.
[40] R. A. Rica, R. Ziano, D. Salerno, F. Mantegazza, M. Z. Bazant, D. Brogioli, *Electrochim. Acta* **2013**, *92*, 304.
[41] J. H. Lee, S. Y. Lee, S. J. Park, *Nanomaterials* **2023**, *13*, 13050817.